Insight from electron density and energy framework analysis on the structural features of F$_x$-TCNQ (x = 0, 2, 4) family of molecules

Rahul Shukla,[a] Christian Ruzié,[b] Guillaume Schweicher,[c] Alan R. Kennedy,[d] Yves H. Geerts,[b] Deepak Chopra[a] and Basab Chattopadhyay[b,e]*

[a]Crystallography and Crystal Chemistry Laboratory, Department of Chemistry, Indian Institute of Science Education and Research Bhopal, Bhopal By-Pass Road, Bhopal, Madhya Pradesh, India 462066, [b]Laboratoire de Chimie des Polymères, CP 206/01, Faculté des Sciences, Université Libre de Bruxelles (ULB), Boulevard du Triomphe, 1050 Brussels, Belgium, [c]Optoelectronics Group, Cavendish Laboratory, University of Cambridge, J. J. Thomson Avenue, Cambridge, CB3 0HE, UK, [d]Department of Pure and Applied Chemistry, University of Strathclyde, 295 Cathedral Street, Glasgow G1 1XL, UK, and [e]Department of Physics, Norwegian University of Science and Technology (NTNU), Høgskoleringen 5, 7491 Trondheim, Norway. *Correspondence e-mail: basab.chattopadhyay@ntnu.no

In this study, the nature and characteristics of the intramolecular and intermolecular interactions in crystal structures of the fluoro-substituted 7,7,8,8-tetracyanoquinodimethane (TCNQ) family of molecules, *i.e.* F$_x$-TCNQ (x = 0, 2, 4), are explored. The molecular geometry of the reported crystal structures is directly dependent on the degree of fluorination in the molecule, which consequently also results in the presence of an intramolecular N≡C···F—C π-hole tetrel bond. Apart from this, the energy framework analysis performed along the respective transport planes provides new insights into the energetic distribution in this class of molecules.

1. Introduction

In the past decade, organic electronics have been the focus of intense scientific interest based on the possibility that they will provide a viable alternative to Si-based devices for large area electronics (Myers & Xue, 2012; Root *et al.*, 2017; Wang *et al.*, 2018). Several attempts has been made to design a highly efficient organic semiconductor (OSC) molecule with high charge carrier mobility (Dou *et al.*, 2015; Horowitz, 1998; Tsutsui *et al.*, 2016; Yang *et al.*, 2018). One of the most important factors that affects the charge carrier mobility of an OSC molecule is the final crystal structure that it adopts in the solid state. High mobilities are observed in compounds having strong π-overlap between molecules in the crystalline state (Wang *et al.*, 2018; Yassar, 2014). In this regard, one of the molecular systems which has garnered significant attention is the fluorinated tetracyanoquinodimethane (F$_x$-TCNQ: x = 0, 2, 4) family of molecules. Among the different derivatives, it is reported that F$_2$-TCNQ shows much higher electron mobility in Organic Field Effect Transistors (OFETs) than TCNQ or F$_4$-TCNQ, up to 25 cm^2 V^{-1} s^{-1} compared with ~0.1 cm^2 V^{-1} s^{-1}. High band-like electron mobility observed in F$_2$-TCNQ was attributed to the presence of planar molecular packing and one molecule in the primitive unit cell (Chernyshov *et al.*, 2017; Krupskaya *et al.*, 2015; Sosorev, 2017). While the molecular packing of these molecules has been discussed previously, the aim of this study was to perform an in-depth quantitative and qualitative investigation into the unique structural and molecular features in this class of molecules.

TCNQ F$_2$-TCNQ

F$_2$'-TCNQ F$_4$-TCNQ
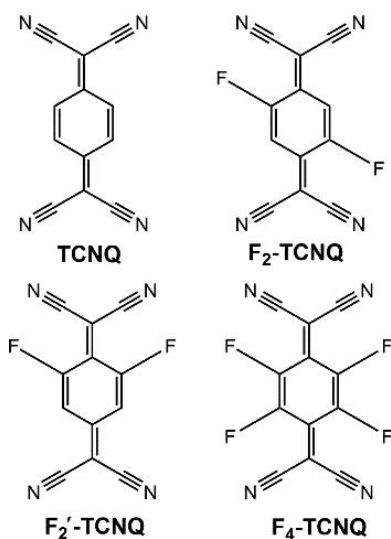
Hence, we present a detailed structural analyses of F_x-TCNQ (x = 0, 2, 4) (Scheme 1) family of molecules. We are also reporting for the first time, the crystal structure of another difluoride derivative *i.e.* 2,6-difluoro-7,7,8,8-tetracyano-quinodimethane (F_2'-TCNQ) (Scheme 1) in this study. We have investigated how the position and extent of fluorination affects the molecular geometry of different TCNQ derivatives. The intramolecular N≡C···F—C π-hole tetrel bond is present as a consequence of fluorination was explored through theoretical X-ray electron density analysis (Hansen & Coppens, 1978). To the best of our knowledge, the analysis of the π-hole tetrel bonds in these molecules is the first of its kind. The overall molecular packing in these molecules was explored by means of energy framework analysis (Turner *et al.*, 2015) and the important intermolecular contacts such as C—H···N and π···π stacking were analysed quantitatively via calculation of the interaction energy (Turner *et al.*, 2014) and topological analysis of the electron density (Bader, 1985. 1991).

Scheme 1
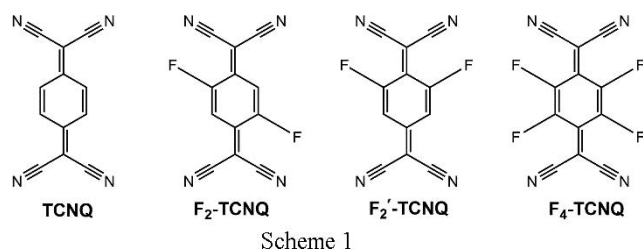
2. Methods

2.1. Materials and crystallization

TCNQ was purchased from Sigma-Aldrich; F_2-TCNQ and F_4-TCNQ were obtained from TCI Europe. All three compounds were used without further purification. F_2'-TCNQ was synthesized by the method reported in the literature (Mochida *et al.*, 1997, 1999). All the compounds were crystallized via the sublimation method.

2.2. X-ray data collection

Single-crystal X-ray diffraction data were collected using a Bruker APEX II diffractometer equipped with a CCD detector using monochromated Mo $K\alpha$ radiation (λ = 0.71073 Å) and φ and ω scans. The data collection for all compounds was carried out at 100 (2) K. The unit-cell measurement, data collection, integration, scaling and absorption corrections for each compound were performed using *APEX3* (Bruker, 2012*a*) software. The intensity data were processed using the *SAINT* (Bruker, 2012*b*) suite of programs. The crystal structures were solved by direct methods using *SIR*92 (Altomare *et al.*, 1994) and refined using the full-matrix least-squares method in *SHELXL*2014 (Sheldrick, 2015) present in the program suite *WinGX* (Version 2014.1; Farrugia, 2012). Empirical absorption correction was applied using *SADABS* (Bruker, 2001). The non-hydrogen atoms were refined anisotropically and the hydrogen atoms bonded to C were set at 1.082 Å for Csp^2—H which corre-

sponds to neutron diffraction data and were refined isotropically. The molecular connectivity and the crystal packing diagrams were generated using *Mercury*3.9 (Macrae *et al.*, 2008). Geometrical calculations were performed using *PARST* (Nardelli, 1995) and *PLATON* (Spek, 2009). The detailed crystallographic data are summarized in Table S1.

2.3. Multipolar modelling

Single-point periodic quantum mechanical calculations were carried out using *CRYSTAL*09 (Dovesi *et al.*, 2005; 2009) at TZVP level of theory (Peintinger *et al.*, 2013), the geometry obtained from the experimental structure determination was used as input data. The shrinking factors (IS1–IS3) along with the reciprocal lattice vectors were set to 4 (27 k-points in the irreducible Brillouin zone). The bielectronic Coulomb and exchange series values for the truncation parameter were set as ITOL1–ITOL4 = 7 and ITOL5 = 14, respectively. The level shifter was set to 0.7 Hartree per cycle for a better convergence. Upon convergence of energy ($\sim$$10^{-6}$ Hartree), the periodic wavefunctions were obtained. Static theoretical structure factors were derived at $\sin(\theta/\lambda)$ = 1.41 Å^{-1} resolution using the XFAC module of *CRYSTAL*09. The theoretical multipolar refinements along with topological analysis were performed with the *MoPro* (Jelsch *et al.*, 2005; Guillot *et al.*, 2014) software package using the Hansen and Coppens (1978) multipole formalism. The atomic positions were held fixed to the values obtained from the experimental structure determination during the spherical atom model refinements. All theoretical structure factors were assigned unit weights during the refinements. The displacement parameters were set to zero to consider a static model and multipolar refinements of the theoretical data were carried out up to the octupole level for non-H atoms and to the dipole level for H atoms. The crystallographic parameters obtained after multipolar refinement confirm the good quality of the model (Table S1). Fig. S1 shows the residual electron density maps [Figs. S1(*a*)–S1(*d*)], 2D deformation density map [Figs. S1(*e*)–S1(*h*)], 2D Laplacian map [Figs. S1(*i*)–S1(*l*)]. Fig. S2 shows the fractal dimensional plots of the respective molecules.

2.4. Topological analysis

The topological analysis was based on Quantum Theory of Atoms In Molecule (QTAIM) developed by Bader (Bader, 1985, 1991). Topological parameters such as the electron density (ρ) and Laplacian ($\nabla^2\rho$) were evaluated at the bond critical point (BCP). At the BCP, the first derivative of the electron density vanishes, *i.e.* $\nabla\rho$ = 0. The Laplacian signifies whether the interaction is a shared interaction ($\nabla^2\rho < 0$) or a closed-shell interaction ($\nabla^2\rho > 0$). Intermolecular/intramolecular interactions are closed-shell interactions with a positive value for both ρ and Laplacian at the BCP (Bader, 1985, 1991).

2.5. Energy framework analysis

We have performed an energy framework analysis (Turner *et al.*, 2015) using *CrystalExplorer* (Version 17.5; Turner *et al.*,

Table 1
Magnitudes of important bond angles present in the reported crystal structures.

Molecule	$\angle A$ (°)	$\angle A'$ (°)	$\angle B$ (°)	$\angle B'$ (°)	$\angle C$ (°)	$\angle C'$ (°)
TCNQ	179.92 (14)	179.33 (12)	179.92 (14)	179.33 (12)	118.59 (10)	118.59 (10)
F_2-TCNQ	179.8 (2)	177.9 (2)	179.8 (2)	177.9 (2)	115.71 (16)	115.71 (16)
F_2'-TCNQ	175.94 (15)	176.18 (15)	176.76 (16)	178.64 (16)	112.99 (12)	118.68 (13)
F_4-TCNQ	174.6 (3)	175.9 (2)	174.6 (3)	175.9 (2)	113.60 (19)	113.60 (19)

2017) on the important intermolecular interactions present along the transport plane in each of the molecules (Fig. 1c). Energy framework analysis has emerged as a useful tool in crystal engineering for correlating different phenomena such as mechanical properties (Turner *et al.*, 2015), polymorphism (Dey *et al.*, 2016) and host–guest interaction (Shi *et al.*, 2015) with three-dimensional topology of interaction energies based on different intermolecular interactions present in molecular crystals. In this analysis, the interaction energies between different molecular pairs are represented via cylindrical tubes connecting the centres of mass of the interacting molecules. The radius of the cylindrical tube is directly proportional to the interaction energies. Further insights can be gained when the energy topology, which is represented by cylindrical tubes, is disintegrated into electrostatic and dispersive components.

2.6. Molecular electrostatic potential map

Molecular electrostatic potential maps for the four molecules were plotted on the Hirshfeld isosurface at the MP2/6-311G** level using *CrystalExplorer* 17 (Turner *et al.*, 2017).

3. Result and discussion

3.1. Molecular geometry and intramolecular N≡C⋯F—C π-hole tetrel bond

Molecular views of all the compounds along with cell parameters and molecular packing are shown in Fig. 1. Complete crystallographic details of all the structures are reported in Table S1. Similar to previously reported structures (Table S2) in the Cambridge Structural Database (Version 5.39; Groom *et al.*, 2016), TCNQ crystallizes in the monoclinic space group $C2/c$ with Z' (number of molecules in the asymmetric unit) = 0.5. F_2-TCNQ crystallizes in the monoclinic space group $C2/m$ with $Z' = 0.25$, F_4-TCNQ crystallizes in the orthorhombic *Pbca* space group with $Z' = 0.5$. We also report, for the first time, the crystal structure of 2,6-difluoro-7,7,8,8-tetracyanoquinodimethane (F_2'-TCNQ), which crystallizes in the monoclinic space group $P2_1/c$ with $Z' = 1$. The effect of fluorination is evident from the analysis of the molecular geometry of the four crystal structures (Fig. 1a). In the case of TCNQ, the magnitude of $\angle A$ (C—C—N) and $\angle A'$ is ~180° (Table 1). As hydrogen is replaced by fluorine, the magnitude of $\angle A'$ decreases to 177.9 (2)° in the case of F_2-TCNQ whereas $\angle A$ largely remains unaffected. In the case of F_2'-TCNQ and F_4-TCNQ, the magnitudes of $\angle A$ and $\angle A'$ decrease to 175.94 (15)° and 176.18 (15)°, and 174.6 (3)° and
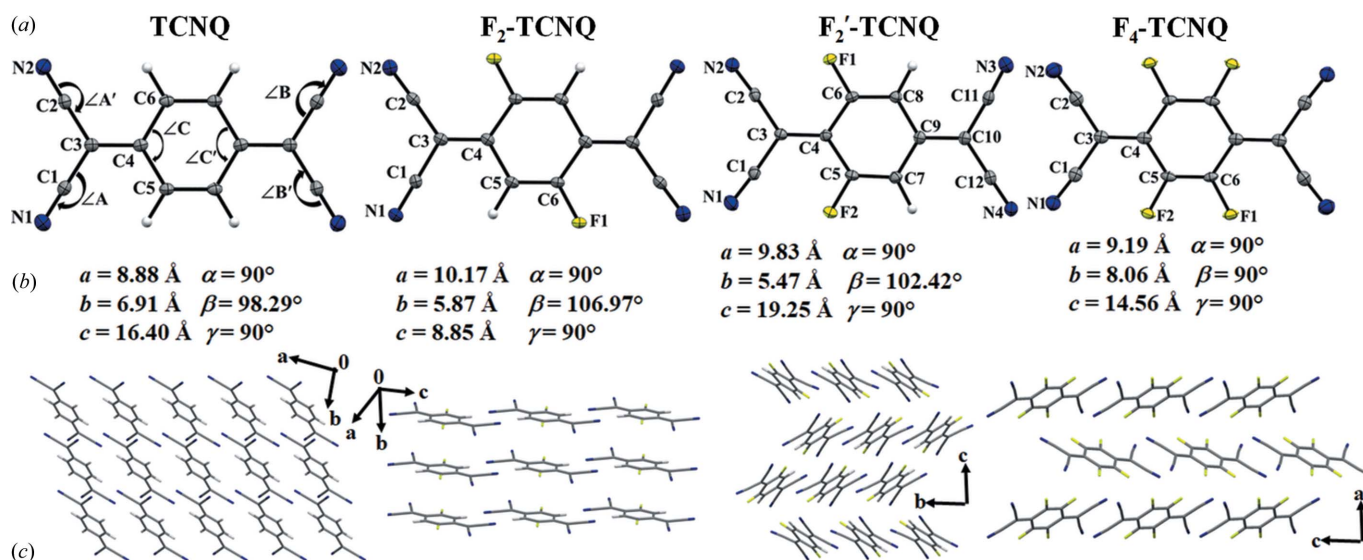

Figure 1
(a) Molecular view of the reported crystal structures drawn with 50% ellipsoidal probability along with the numbering scheme and important bond angles. (b) Cell parameters. (c) Molecular packing along the transport plane: TCNQ (*ab*-plane), F_2-TCNQ ($\bar{2}00$), F_2'-TCNQ (100) and F_4-TCNQ (*ac*-plane).

175.9 (2)°, respectively (Table 1). Except for F_2'-TCNQ, $\angle A = \angle B$ and $\angle A' = \angle B'$ due to the presence of crystallographically imposed symmetry. The magnitudes of $\angle B$ and $\angle B'$ in F_2'-TCNQ are 176.76 (16)° and 178.64 (16)°, respectively.

The presence of an intramolecular π-hole interaction, where the lone pair (lp) of F interacts with the electron-deficient region (π-hole) of the CN bond resulting in the formation of an intramolecular lp$\cdots\pi$ interaction [Figs. 2(a)–2(d)]. It was also substantiated via quantitative inputs from the topological parameters characterized by the finite positive values of the electron density and the Laplacian at the (3, −1) F$\cdots$C(π) bond critical point between the fluorine and the carbon atom [Figs. 2(a)–2(d)]. The magnitude of ρ ranges from 0.089 to 0.108 e Å^{-3} while the magnitude of $\nabla^2\rho$ ranges from 1.53 to 1.78 e Å^{-5}. The relatively small value of ρ and the positive value of $\nabla^2\rho$ establishes the closed-shell nature of the interaction (Bader, 1985, 1991). The large magnitude of these topological parameters indicates the highly stabilizing nature of these intramolecular interactions (Table 2). The π-hole tetrel bonding nature of this intramolecular interaction is further supported by 2D deformation density maps where the charge-concentrated (CC) region on fluorine is clearly directed towards the charge-depleted (CD) region on the carbon atom of the C$\equiv$N bond [Figs. 2(e)–2(h)]. It is important here to note that N$\equiv$C$\cdots$F—C π-hole tetrel bonds are

Table 2
Geometrical and topological parameters at intramolecular F$\cdots$C bond critical point.

Interaction	$d_{F\cdots C}$ (Å)	C—F$\cdots$C (°)	R_{ij} (Å)	ρ (e Å^{-3})	$\nabla^2\rho$ (e Å^{-5})
F_2-TCNQ					
F1$\cdots$C2	2.647 (2)	92	2.658	0.089	1.53
F_2'-TCNQ					
F1$\cdots$C2	2.563 (1)	94	2.582	0.108	1.78
F2$\cdots$C1	2.598 (2)	93	2.617	0.096	1.62
F_4-TCNQ					
F1$\cdots$C2	2.607 (2)	91	2.616	0.094	1.63
F2$\cdots$C1	2.599 (2)	92	2.604	0.099	1.65

uncommon and their presence might lead to new possibilities for understanding chemical reactivity in such classes of compounds.

Apart from the deviation in the C—C$\equiv$N bond, the angular deviation was also observed in the hexadiene ring. $\angle C$ (Fig. 1) was observed to be 118.59 (10)°, 115.71 (16)° and 113.60 (19)° for TCNQ, F_2-TCNQ and F_4-TCNQ, respectively (Table 1). The corresponding $\angle C$ and $\angle C'$ angles in F_2'-TCNQ were calculated to be 112.99 (12)° and 118.68 (13)°, respectively, which clearly shows the effect of fluorination on the alteration in the observed molecular geometry from the ideal value of 120°.

3.2. Molecular packing along the transport plane

In this study, we have performed the packing analysis exclusively along the transport plane. The transport plane corresponds to the surfaces where the accumulation of electrons takes place in the FET devices. The transport planes for TCNQ (ab-plane), F_2-TCNQ ($\bar{2}00$) and F_4-TCNQ (ac-plane) molecules were reported recently (Krupskaya $et\ al.$, 2015) and we have utilized the same planes for this analysis. Since the transport plane for F_2'-TCNQ is not known, the crystal morphology [using BFDH morphology (Donnay & Harker, 1937) module in $Mercury$3.9] was obtained and (100) emerges as a potential transport plane due to the presence of well-defined molecular layers similar to those observed for the other three structures (Fig. S3). In addition to this, we have performed topological analysis along the transport plane in order to analyse the features of different interactions such as hydrogen bonds and π–π stacking interactions.

3.2.1. Packing analysis of TCNQ and F_2-TCNQ. In both TCNQ and F_2-TCNQ, the significant electrostatic contribution is present along the transport plane due to the presence of short and moderately strong C—H$\cdots$N interactions [motif I in TCNQ and motif II in F_2-TCNQ; Table S6; Figs. 3(a) and 3(e)], which forms a 1D molecular chain [Figs. 4(a)–4(f)]. The value of ρ has magnitudes of 0.057 e Å^{-3} (TCNQ) and 0.051 e Å^{-3} (F_2-TCNQ), while $\nabla^2\rho$ has magnitudes of 1.10 e Å^{-5} (TCNQ) and 0.72 e Å^{-5} (F_2-TCNQ) at the (3,−1) BCP of the C—H$\cdots$N interaction. Both structures are also supported by the presence of type I N$\cdots$N contacts as confirmed by the topological analysis [Figs. 3(a) and 3(e), Table S7]. This is in accordance with the observation made in a previous study
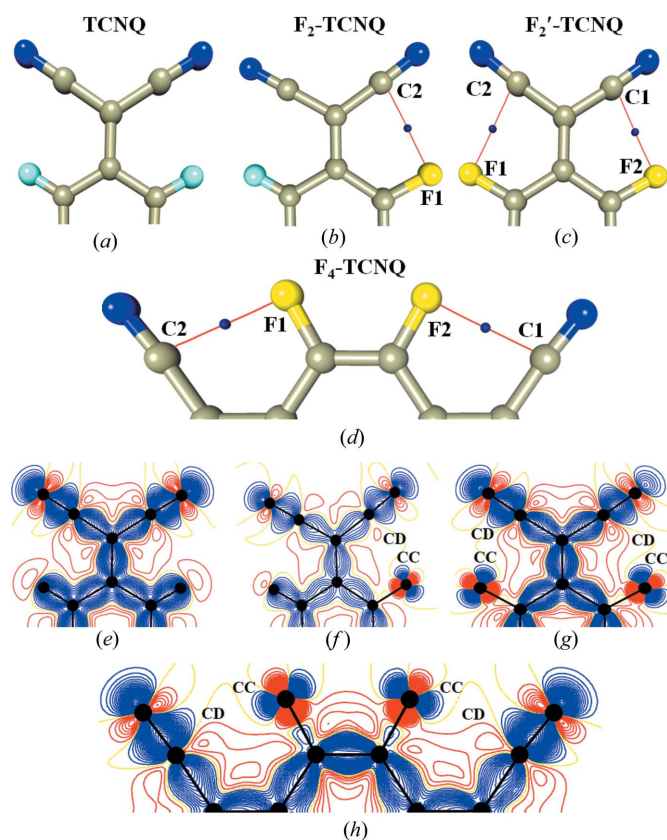

Figure 2
(a–d) Molecular plots depicting the presence of F$\cdots$C (π) (3,−1) bond critical point. (e–h) 2D deformation density plots showing the presence of charge-concentrated (blue) and charge-depleted (red) regions between the interacting atoms.

(Chernyshov *et al.*, 2017). Also in both structures, the similar chain formed by C—H···N interactions are interconnected to each other via two different molecular stacking motifs (motifs II and III in TCNQ; motifs I and III in F_2-TCNQ; Fig. 3).

In the case of TCNQ, the similar chains formed by C—H···N interaction are interconnected to each other via two dispersion dominant stacking interactions [motif II, -23.2 kJ mol^{-1}; motif III, -17.4 kJ mol^{-1}; Fig. 4(*a*)]. These stacking interactions are oriented along *a* and *b* axes while the electrostatically driven motif I is oriented in between the stacking motif. Because of this, the tube representing the dominant electrostatic component roughly makes an angle of $\sim 45°$ with the dominant dispersive component (Fig. 4*d*).

In the case of F_2-TCNQ, the similar chains formed by C—H···N interaction along the *a* axis (motif II, -26.2 kJ mol^{-1}) are interconnected to each other by two stacking motifs along the *b* axis (motif I, -28.8 kJ mol^{-1}; motif III, -17.9 kJ mol^{-1}). Thus the total interaction energy (IE) along the *b* axis is -46.8 kJ mol^{-1}, whereas along the *a* axis the magnitude is -23.2 kJ mol^{-1}. Of the two stacking motifs, one is highly dispersive in nature ($\sim 68\%$) whilst the other has a significant electrostatic contribution ($\sim 49\%$) (Table S7) also. However, the magnitudes of the electrostatic (-13.7 kJ mol^{-1}) and

dispersive (-14.1 kJ mol^{-1}) contributions in motif III are significantly lower than the dominant electrostatic (-32.9 kJ mol^{-1}) contribution in motif II and dispersion (-28.7 kJ mol^{-1}) contribution in motif I. Interestingly, topological analysis of motif I of F_2-TCNQ reveals the presence of a C—F···F—C interaction (Fig. 3*d*). This shows that π···π interactions in stacking motifs are also assisted by other types of intermolecular interactions. Only in the case of F_2-TCNQ are the tubes representing the dominant electrostatic and dispersion are approximately orthogonal to each other (Fig. 4*h*). In a recent review, it was reported that electron conductivity is typically high in the direction of the strong intermolecular interactions (Wang *et al.*, 2018). In the case of F_2-TCNQ also, the total interaction strength was found to be significantly higher in the π-stacking direction. Another important observation is that the overall contribution of electrostatic energy (-59.8 kJ mol^{-1}) was more than dispersion energy (-53.3 kJ mol^{-1}) along the transport plane in the case of F_2-TCNQ, while dispersion was more dominant in the structures of the other three species (Table S7).

3.2.2. Packing analysis of F_4-TCNQ. While the molecular packings of TCNQ, F_2-TCNQ, and F_4-TCNQ along the transport plane are uniform [Figs. 4(*a*)–4(*i*)] wherein a specific
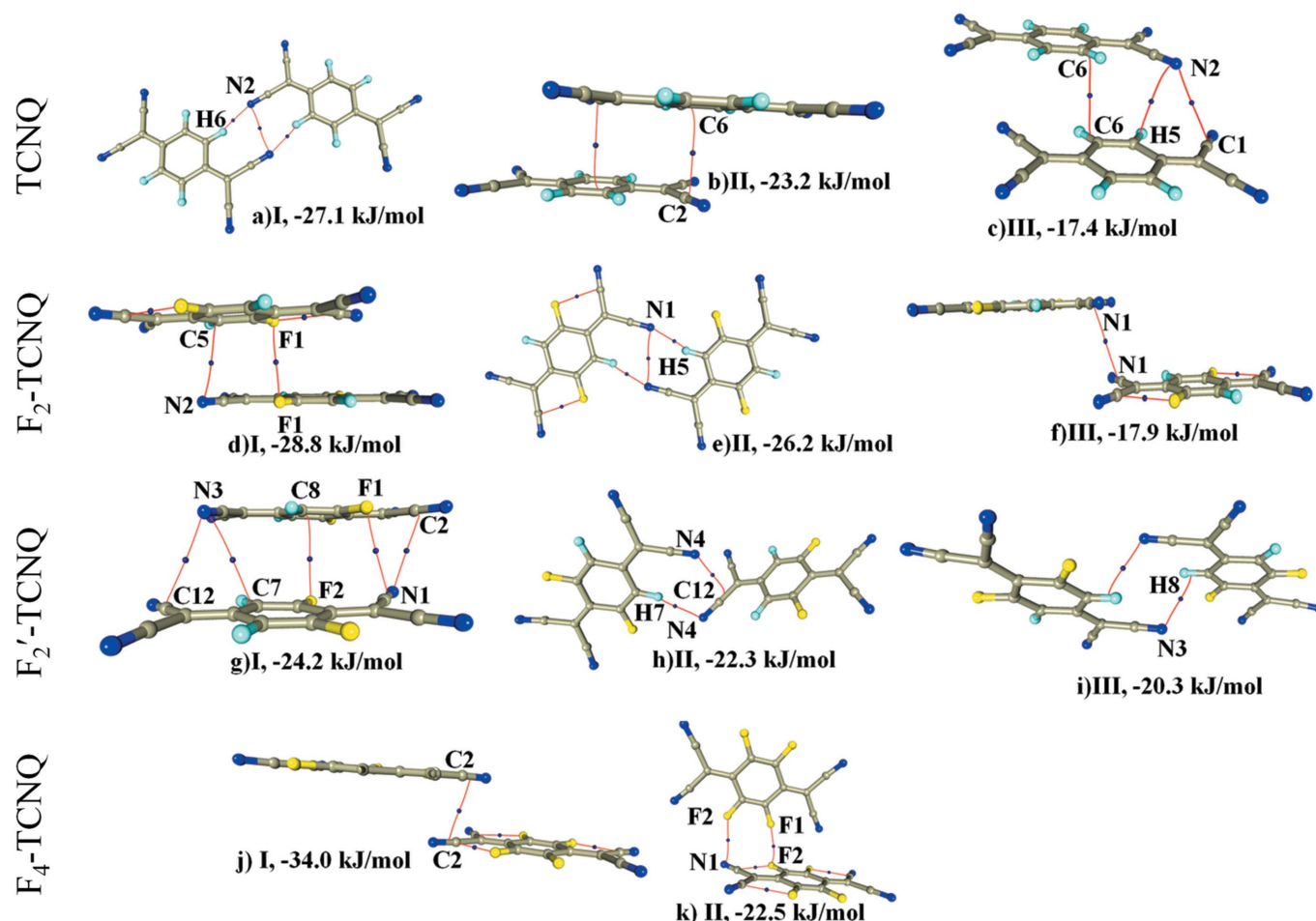

Figure 3
Different molecular motifs present along the transport plane of (*a*–*c*) TCNQ, (*d*–*f*) F_2-TCNQ, (*g*–*i*) F_2'-TCNQ and (*j*–*k*) F_4-TCNQ

arrangement of molecule is present in two dimensions, the differences arising on account of the role played by the combination of electrostatic and dispersive forces acting between the molecules. The molecular packing along the c axis in F_4-TCNQ [Fig. 4(i)] is governed by molecular stacking [motif I, IE = -34.0 kJ mol^{-1}; Fig. 3(j)] with significant contribution from both electrostatic ($\sim$54%) and dispersion components ($\sim$46%) (Table S7). This stacking layer is interconnected to another similar layer down the a axis via dispersive ($\sim$67%) F$\cdots$F and F$\cdots$N interactions [motif II, -22.5 kJ mol^{-1}; Fig. 3(k)]. The absence of a significantly electrostatic dominant interaction (where the contribution of the electrostatic component is significantly greater than the dispersive component towards stabilization) (Table S6) causes both the electrostatic and dispersion components (Fig. 4l) to be oriented in a non-orthogonal manner along the c axis.

3.2.3. Packing analysis of F_2'-TCNQ. The energy framework analysis of F_2'-TCNQ reveals that it has non-uniform packing [Figs. 4(m)–4(o)] along the expected transport plane compared with the other three molecules which have uniform packing [Figs. 4(a)–4(i)]. In the case of F_2'-TCNQ, the molecular layer present along the b axis is formed by a molecular stacking interaction (motif I, -24.2 kJ^{-1}, Table S7) with 81% contribution from the dispersion component towards stabilization, The topological analysis reveals the presence of multiple $\pi\cdots\pi$ and lp$\cdots\pi$ interactions in motif I (Fig. 3g). This molecular layer is then connected to another similar layer along the c axis via the electrostatic-dominant (62%) moderately strong C—H$\cdots$N ($d_{H\cdots N}$ = 2.49 Å; $\angle$C—H$\cdots$N = 166°) and N4$\cdots$C12 lp$\cdots\pi$ interactions (motif II, IE = -22.3 kJ mol^{-1}) giving rise to a T-shaped dimer (Fig. 4m).The molecular packing is then further extended along the c axis via another stacking interaction (motif III, -20.3 kJ mol^{-1}). Interestingly, the topological analysis revealed the presence of a hydrogen bond due to the presence of a (3,-1) BCP between H8 and N3 [$d_{H\cdots N}$ = 2.82 Å; $\angle$C—H$\cdots$N = 105°; Fig. 3(i)]. This also explains the origin of a substantial electrostatic component in this stacking motif (Table S6). Hence, the molecular packing along the expected transport plane of F_2'-TCNQ is stabilized by two alternate types of molecular layers which results in non-uniform packing.
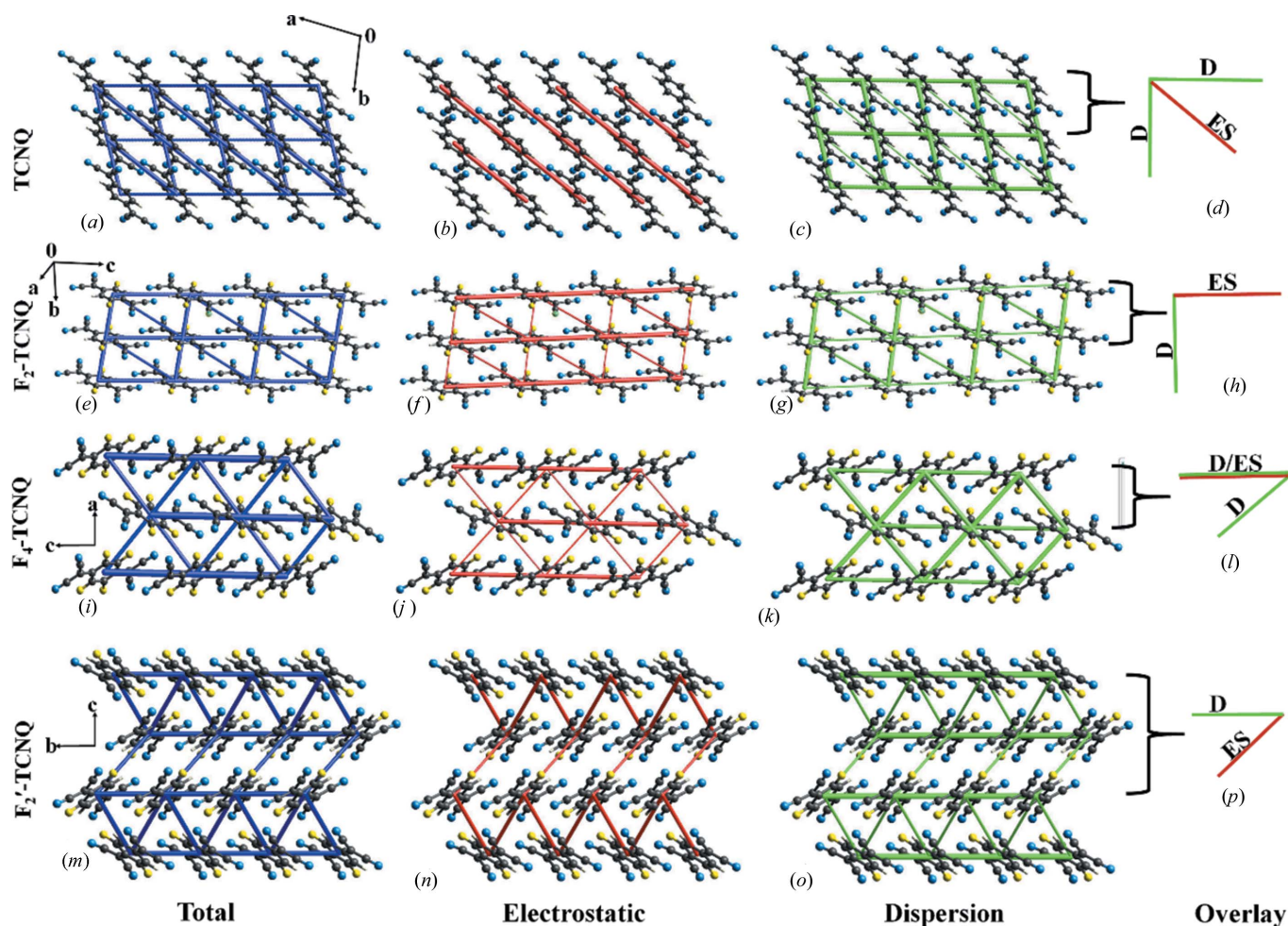

Figure 4
Total energy contribution in (a) TCNQ, (e) F_2-TCNQ (i) F_4-TCNQ, (m) F_2'-TCNQ. Electrostatic energy contribution in (b) TCNQ, (f) F_2-TCNQ, (j) F_4-TCNQ, (n) F_2'-TCNQ. Dispersion energy contribution in (c) TCNQ, (g) F_2-TCNQ, (k) F_4-TCNQ, (o) F_2'-TCNQ. Overlay of the dominant contributor along the transport plane in (d) TCNQ, (h) F_2-TCNQ, (l) F_4-TCNQ, (p) F_2'-TCNQ. ES stands for electrostatic and D stands for the dispersive component.
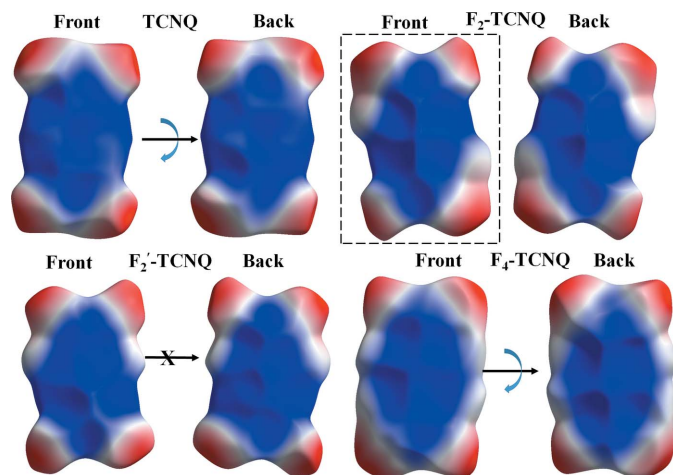
Figure 5
Molecular electrostatic potential (MESP) maps of the four crystal structures drawn on Hirshfeld isosurface at ±0.03 contour level. Red represents negative and blue represents positive electrostatic potentials (both front and back view). The arrows between the front and back of a given molecule in TCNQ and F4-TCNQ show that the electrostatic potential distribution of the two faces are similar but are oriented in the opposite direction. The cross between the front and back of F2′-TCNQ shows that the electrostatic potential distribution in the front and back of the molecule is not similar with respect to each other. The dotted lines shown in the front view of F2-TCNQ represent the existence of a mirror plane due to which the electrostatic potential distribution on the front and back of F2-TCNQ is same.

3.3. Electrostatic potential maps

In all four molecules (see Fig. 5) the positive electrostatic region (in blue) belongs to the quinodimethane region and the hydrogen atoms present in the molecule while the negative electrostatic region belonged to the cyano region (in red). Despite its high electronegativity, the negative electrostatic region on fluorine was significantly less than that of the cyano group. This observation is consistent with the observation made in a previous study (Ji *et al.*, 2018). However, the most important aspect of these MESP maps is how the electrostatic potential distribution exists in these molecules. In the case of TCNQ and F_4-TCNQ (Fig. 5), the electrostatic distributions for both sides of the molecules are the same but are oriented in opposite directions. In the case of F_2-TCNQ, the front and back sides of the molecule are connected by a mirror image which is responsible for the similar distribution of the electrostatic potential above and below the plane. This unique distribution of electrostatic potential exclusively in F_2-TCNQ separates it from the other molecules investigated in this study. In the case of F_2'-TCNQ, the electrostatic potential distribution on both sides of the molecule is completely different with no relation between the electrostatic potential distributions on both sides.

4. Summary

In this study it is observed that the degree of fluorination in the F_x-TCNQ (x = 0, 2, 4) family of molecules affects the

geometry in the molecules. Fluorination also results in the presence of an intramolecular $N\equiv C\cdots F-C$ interaction which acts as a conformational lock. The theoretical charge density analysis confirms this interaction to be a proper donor–acceptor interaction where the lone pairs of fluorine interact with the electron-deficient region of the $C\equiv N$ bond. Topological analysis establishes the presence of a $(3,-1)$ $F\cdots C$ bond critical point and hence this interaction can be categorized as a π-hole tetrel bond. The energy framework analysis revealed the energetic distribution along the transport plane in the reported molecules. The analysis showed that F_2-TCNQ, which has exceptionally high charge carrier mobility compared with other derivatives, also has unique structural features. All the molecules have significant contribution from electrostatic and dispersion components towards the stabilization of the molecular packing. However, only in the case of F_2-TCNQ were the tubes representing the dominant electrostatic and dispersion contributions orthogonal to each other. The molecular electrostatic potential map also reveals that F_2-TCNQ has a unique electrostatic distribution compared with other molecules.

References

Altomare, A., Cascarano, G., Giacovazzo, C., Guagliardi, A., Burla, M. C., Polidori, G. & Camalli, M. (1994). *J. Appl. Cryst.* **27**, 435–435.
Bader, R. F. W. (1985). *Acc. Chem. Res.* **18**, 9–15.
Bader, R. F. W. (1991). *Chem. Rev.* **91**, 893–928.
Bruker (2001). *SADABS.* Bruker AXS Inc., Madison, WI, USA.
Bruker (2012*a*). *APEX*3. Bruker AXS Inc., Madison, WI, USA.
Bruker (2012*b*). *SAINT.* Bruker AXS Inc., Madison, WI, USA.
Chernyshov, I. Y., Vener, M. V., Feldman, E. V., Paraschuk, D. Y. & Sosorev, A. Y. (2017). *J. Phys. Chem. Lett.* **8**, 2875–2880.
Dey, D., Thomas, S. P., Spackman, M. A. & Chopra, D. (2016). *Chem. Commun.* **52**, 2141–2144.
Donnay, J. D. H. & Harker, D. (1937). *Am. Mineral.* **22**, 446–467.
Dou, J.-H., Zheng, Y.-Q., Yao, Z.-F., Yu, Z.-A., Lei, T., Shen, X., Luo, X.-Y., Sun, J., Zhang, S.-D., Ding, Y.-F., Han, G., Yi, Y., Wang, J.-Y. & Pei, J. (2015). *J. Am. Chem. Soc.* **137**, 15947–15956.
Dovesi, R., Orlando, R., Civalleri, B., Roetti, C., Saunders, V. R. & Zicovich-Wilson, C. M. (2005). *Z. Kristallogr.* **220**, 571–573.
Dovesi, R., Saunders, V. R., Roetti, C., Orlando, R., Zicovich-Wilson, C. M., Pascale, F., Civalleri, B., Doll, K., Harrison, N. M., Bush, I. J., D'Arco, P. & Llunell, M. (2009). *CRYSTAL09* User's Manual. University of Turin, Italy.
Farrugia, L. J. (2012). *J. Appl. Cryst.* **45**, 849–854.

Groom, C. R., Bruno, I. J., Lightfoot, M. P. & Ward, S. C. (2016). *Acta Cryst.* B**72**, 171–179.

Guillot, B., Enrique, E., Huder, L. & Jelsch, C. (2014). *Acta Cryst.* A**70**, C279–C279.

Hansen, N. K. & Coppens, P. (1978). *Acta Cryst.* A**34**, 909–921.

Horowitz, A. (1998). *Adv. Mater.* **10**, 365–377.

Jelsch, C., Guillot, B., Lagoutte, A. & Lecomte, C. (2005). *J. Appl. Cryst.* **38**, 38–54.

Ji, L. F., Fan, J., Zhang, S. F. & Ren, A. M. (2018). *Phys. Chem. Chem. Phys.* **20**, 3784–3794.

Krupskaya, Y., Gibertini, M., Marzari, N. & Morpurgo, A. F. (2015). *Adv. Mater.* **27**, 2453–2458.

Macrae, C. F., Bruno, I. J., Chisholm, J. A., Edgington, P. R., McCabe, P., Pidcock, E., Rodriguez-Monge, L., Taylor, R., van de Streek, J. & Wood, P. A. (2008). *J. Appl. Cryst.* **41**, 466–470.

Mochida, T., Hasegawa, T., Kagoshima, S., Sugiura, S. & Iwasa, Y. (1997). *Synth. Met.* **86**, 1797–1798.

Mochida, T., Moriyama, H., Hasegawa, T., Kondo, R., Kagoshima, S. & Iwasa, Y. (1999). *Synth. Met.* **102**, 1678–1679.

Myers, J. D. & Xue, J. (2012). *Polym. Rev.* **52**, 1–37.

Nardelli, M. (1995). *J. Appl. Cryst.* **28**, 659.

Peintinger, M. F., Oliveira, D. V. & Bredow, T. (2013). *J. Comput. Chem.* **34**, 451–459.

Root, S. E., Savagatrup, S., Printz, A. D., Rodriquez, D. & Lipomi, D. J. (2017). *Chem. Rev.* **117**, 6467–6499.

Sheldrick, G. M. (2015). *Acta Cryst.* C**71**, 3–8.

Shi, M. W., Thomas, S. P., Koutsantonis, G. A. & Spackman, M. A. (2015). *Cryst. Growth Des.* **15**, 5892–5900.

Sosorev, A. Y. (2017). *Phys. Chem. Chem. Phys.* **19**, 25478–25486.

Spek, A. L. (2009). *Acta Cryst.* D**65**, 148–155.

Tsutsui, Y., Schweicher, G., Chattopadhyay, B., Sakurai, T., Arlin, J., Ruzié, C., Aliev, A., Ciesielski, A., Colella, S., Kennedy, A. R., Lemaur, V., Olivier, Y., Hadji, R., Sanguinet, L., Castet, F., Osella, S., Dudenko, D., Beljonne, D., Cornil, J., Samorì, P., Seki, S. & Geerts, Y. H. (2016). *Adv. Mater.* **28**, 7106–7114.

Turner, M. J., Grabowsky, S., Jayatilaka, D. & Spackman, M. A. (2014). *J. Phys. Chem. Lett.* **5**, 4249–4255.

Turner, M. J., McKinnon, J. J., Wolff, S. K., Grimwood, D. J., Spackman, P. R., Jayatilaka, D. & Spackman, M. A. (2017). *CrystalExplorer17*. University of Western Australia, Australia.

Turner, M. J., Thomas, S. P., Shi, M. W., Jayatilaka, D. & Spackman, M. A. (2015). *Chem. Commun.* **51**, 3735–3738.

Wang, C., Dong, H., Jiang, L. & Hu, W. (2018). *Chem. Soc. Rev.* **47**, 422–500.

Yang, J., De, S., Campbell, J. E., Li, S., Ceriotti, M. & Day, G. M. (2018). *Chem. Mater.* **30**, 4361–4371.

Yang, A. (2014). *Polym. Sci. Ser. C*, **56**, 4–19.